PERGAMON Computers and Mathematics with Applications 44 (2002) 25–49

An International Journal
computers & mathematics
with applications

www.elsevier.com/locate/camwa

Unsplit Algorithms for Multidimensional Systems of Hyperbolic Conservation Laws with Source Terms

M. V. PAPALEXANDRIS*, A. LEONARD AND P. E. DIMOTAKIS
Graduate Aeronautical Laboratories, California Institute of Technology
Pasadena, CA 91125, U.S.A.
milto@hive.jpl.nasa.gov

(Received June 2001; revised and accepted September 2001)

Abstract—This work describes an unsplit, second-order accurate algorithm for multidimensional systems of hyperbolic conservation laws with source terms, such as the compressible Euler equations for reacting flows. It is a MUSCL-type, shock-capturing scheme that integrates all terms of the governing equations simultaneously, in a single time-step, thus avoiding dimensional or time-splitting. Appropriate families of space-time manifolds are introduced, along which the conservation equations decouple to the characteristic equations of the corresponding 1-D homogeneous system. The local geometry of these manifolds depends on the source terms and the spatial derivatives of the flow variables. Numerical integration of the characteristic equations is performed along these manifolds in the upwinding part of the algorithm. Numerical simulations of two-dimensional detonations with simplified kinetics are performed to test the accuracy and robustness of the algorithm. These flows are unstable for a wide range of parameters and may exhibit chaotic behavior. Grid-convergence studies and comparisons with earlier results, obtained with traditional schemes, are presented.

Keywords—Unsplit schemes, Conservation laws, Hyperbolic PDEs, Source terms, Detonations.

1. INTRODUCTION

Considerable amount of work had been devoted to the theoretical study of systems of hyperbolic conservation laws. Most of the effort was focused in systems with two independent variables. These variables were, usually, a time and a space variable. As a result of this effort, it became possible to establish the existence and uniqueness of weak solutions for such systems and to derive important properties of these solutions, such as their asymptotic behavior, see [1,2]. The theoretical developments were followed by the design of accurate algorithms for the numerical approximation of these solutions, such as the MUSCL scheme [3], the ENO schemes [4], the PPM method [5], and others. These algorithms take into account the presence of discontinuities in the solution by solving a 1-D Riemann problem at each computational cell interface. The concepts

*Author to whom all correspondence should be addressed. Jet Propulsion Laboratory, Mail Code: 306-336, California Institute of Technology, Pasadena, CA 91109, U.S.A.
This work is sponsored by the Air Force Office of Scientific Research Grant No. F49620-94-1-0353 and F49626-93-1-00338, whose support is gratefully acknowledged.

0898-1221/02/$ - see front matter Typeset by AMS-TEX
PII: S0898-1221(02)00128-1

of characteristics and Riemann invariants played a significant role in both the theoretical and computational developments on the field.

The extension, however, of theoretical results to systems with more than two independent variables proved to be a very difficult task. The complicated topology of the discontinuous solutions admitted by such systems has not allowed, so far, global existence theories. Furthermore, general solution for the multidimensional Riemann problem is not yet available. This does not allow a straightforward extension of the various shock algorithms in many dimensions. A robust, and in many cases efficient, way to overcome this difficulty is to employ dimensional splitting. Such schemes advance the solution to the next time-step through a series of one-dimensional computations on each spatial dimension.

Algorithms that do not employ splitting have also been presented by various authors in the past. Such algorithms include the characteristic-based schemes of Deconick *et al.* [6] and others. Colella [7] developed an unsplit scheme by considering the characteristic form of the multidimensional equations at the cell interfaces. LeVeque [8] designed a finite-volume method based on one-dimensional normal and tangential Riemann problems. More recently, Dai and Woodward [9] proposed a scheme based on a single-step Eulerian formulation of the discretized equations.

An alternative approach for solving homogeneous systems in many spatial dimensions was introduced by Lappas *et al.* [10], who developed an unsplit MUSCL-type scheme for the 2-D compressible Euler equations. In their analysis, a general methodology is developed that defines manifolds in space-time, dubbed, "Riemann invariant manifolds", along which the equations are decomposed into the same scalar fields as in the one-dimensional case and then solved numerically.

The problems arising in the numerical solution of nonlinear hyperbolic equations become more complicated when source terms are present because of the development of a much larger number of spatial and temporal scales. The source terms are stiff for most practical applications and this makes the integration of the equations even more difficult. The conventional method for solving such systems is to introduce time splitting for the source terms, i.e., integration of the source term in an intermediate time-step, in addition to dimensional splitting.

The present work describes the generalization of the algorithm proposed by Papalexandris *et al.* [11] to multidimensional systems with source terms. A new family of space-time manifolds is introduced along which the system of equations can be decomposed into the characteristic ODEs for the corresponding one-dimensional homogeneous case. These manifolds are the Riemann invariant manifolds for the system under consideration, equivalent to the ones defined in [10] for the inert case. This particular decomposition is then employed in the upwinding step of a MUSCL-type scheme that integrates all the terms of the equations simultaneously, in a single and fully-coupled time-step. Neither time splitting nor dimensional splitting is performed. In the first part of this paper, the construction of the invariant manifolds and a detailed description of the proposed unsplit algorithm are presented. The second part contains numerical tests on unsteady, two-dimensional detonations. Discussion of the results is included, with emphasis on the instability mechanisms of such flows. Comparisons with results in the literature are also made.

2. RIEMANN INVARIANT MANIFOLDS OF THE REACTIVE EULER EQUATIONS

Consider the Euclidean space-time of N spatial dimensions, $t \times \Re^N$, and the following system of M equations, satisfied at each point $(t, \mathbf{x}) = (t, x_1, \ldots, x_N)$ of $t \times \Re^N$:

$$\frac{\partial \mathbf{U}}{\partial t} + A_j(\mathbf{U}) \frac{\partial \mathbf{U}}{\partial x_j} = \mathbf{G}, \qquad j = 1, \ldots, N. \tag{1}$$

In the quasilinear system above, $\mathbf{U}(t, \mathbf{x}) = [u_1(t, \mathbf{x}), \ldots, u_M(t, \mathbf{x})]$ is the solution vector, and $\mathbf{G}(\mathbf{U}, t, \mathbf{x}) = [g_1(\mathbf{U}, t, \mathbf{x}), \ldots, g_M(\mathbf{U}, t, \mathbf{x})]$ is the vector of the source terms. $A_j(\mathbf{U})$, $j = 1, \ldots, N$, are $M \times M$ matrices. Summation notation is implied for repeated indices.

The Cauchy initial value problem for this system amounts to specifying data (referred to as Cauchy data) at points on some initial N-dimensional submanifold of $t \times \Re^N$, $\mathcal{S}$, and determining $\mathbf{U}$ that satisfies (1) off this manifold. The idea behind the hyperbolicity of a quasi-linear system is that the Cauchy problem be well posed for it, i.e., there exists a unique solution that depends continuously on the data specified on $\mathcal{S}$. It is interesting to see how the terms of system (1) can be rearranged so that the derivative of $\mathbf{U}$ normal to $\mathcal{S}$ (exterior derivative) can be expressed in terms of the Cauchy data and its derivatives in $\mathcal{S}$ (interior derivatives).

The way to do this is to consider a coordinate transformation and replace $(t, \mathbf{x})$ by a new vector, $\boldsymbol{\phi} = [\phi_0, \ldots, \phi_N]$. The components $\phi_i(t, \mathbf{x})$, $i = 0, \ldots, N$, are assumed to be differentiable functions of their arguments. Keep the variable t unchanged, i.e., $\phi_0 = t$, and assume that the manifold $\mathcal{S}$ is associated with one particular coordinate, say ϕ_N. The following equation is then used to define the manifold $\mathcal{S}$

$$\phi_N(t, \mathbf{x}) = 0. \tag{2}$$

The other coordinates $\phi_i(t, \mathbf{x})$, $i = 1, \ldots, N-1$, can be selected arbitrarily, provided that the Jacobian of the coordinate transformation,

$$J = \frac{\partial(t, x_1, \ldots, x_N)}{\partial(\phi_0, \ldots, \phi_N)}, \tag{3}$$

is nonvanishing at the points of interest, i.e., in the vicinity of $\mathcal{S}$. Then system (1) becomes

$$\left(I\frac{\partial \phi_N}{\partial t} + A_j \frac{\partial \phi_N}{\partial x_j}\right)\frac{\partial \mathbf{U}}{\partial \phi_N} + \left(I\frac{\partial \phi_i}{\partial t} + A_j \frac{\partial \phi_i}{\partial x_j}\right)\frac{\partial \mathbf{U}}{\partial \phi_i} = \mathbf{G}(\mathbf{U}, t, \mathbf{x}). \tag{4}$$

By making the substitutions

$$\begin{aligned} \boldsymbol{\Lambda} &\equiv I\frac{\partial \phi_N}{\partial t} + A_j \frac{\partial \phi_N}{\partial x_j}, \\ \mathbf{R} &\equiv \left(I\frac{\partial \phi_i}{\partial t} + A_j \frac{\partial \phi_i}{\partial x_j}\right)\frac{\partial \mathbf{U}}{\partial \phi_i} - \mathbf{G}, \end{aligned} \tag{5}$$

system (4) yields

$$\boldsymbol{\Lambda}\frac{\partial \mathbf{U}}{\partial \phi_N} + \mathbf{R} = \mathbf{0}. \tag{6}$$

Given Cauchy data on $\mathcal{S}$, all tangential derivatives $\frac{\partial \mathbf{U}}{\partial \phi_i}$, $i = 0, \ldots, N-1$, are known. Only the $\mathcal{S}$-normal derivative, i.e., the exterior derivative, is not known. It can be evaluated, however, by equation (6) provided that $\boldsymbol{\Lambda}^{-1}$ exists. This condition implies that the following relation must hold on a given point P of $\mathcal{S}$:

$$Q(P; \mathbf{n}, \lambda) \equiv \det(\boldsymbol{\Lambda}) \neq 0. \tag{7}$$

Furthermore, let $\nabla\phi_N$ be the spatial gradient of ϕ_N and define

$$\begin{aligned} \lambda &\equiv \frac{-\frac{\partial \phi_N}{\partial t}}{|\nabla \phi_N|}, \\ \mathbf{n} &\equiv \frac{\nabla \phi_N}{|\nabla \phi_N|}. \end{aligned} \tag{8}$$

Substituting in the expression for $Q(P; \mathbf{n}, \lambda)$, one finds that

$$Q(P; \mathbf{n}, \lambda) = \det(-\lambda I + n_j A_j). \tag{9}$$

This is a homogeneous polynomial of degree M in the quantities $(\lambda, n_1, \ldots, n_N)$ and a first-order differential equation for $\phi_N(t, \mathbf{x})$.

The surfaces along which this polynomial equals zero are the characteristic surfaces. The differential equation that holds on a particular characteristic surface can be found by taking the inner product of the original system with the appropriate left eigenvector, $\mathbf{l}_k$,

$$\mathbf{l}_k \cdot \frac{\partial \mathbf{U}}{\partial t} + \mathbf{l}_k \cdot \left(A_j \frac{\partial \mathbf{U}}{\partial x_j} - \mathbf{G} \right) = 0, \qquad k = 1, \ldots, M. \tag{10}$$

The system of first-order, quasi-linear equations (1) is defined to be hyperbolic at a point P in the space-time $t \times \Re^N$, if real characteristic surfaces pass through this point, i.e., if the zeros λ_k of $Q(P; \mathbf{n}, \lambda)$ are all real, and if its right eigenvectors $\mathbf{r}_k$, satisfying

$$(-\lambda_k I + n_j A_j)\, \mathbf{r}_k = 0, \qquad k = 1, \ldots, M, \tag{11}$$

(no summation on k), span the space E^M. The property of hyperbolicity as formulated above is a local property and depends on both the point P and the Cauchy data prescribed initially.

Consider now a simple model of chemical interaction of two calorically perfect gases, $A \rightarrow B$, assuming one-step, irreversible, Arrhenius kinetics, and the absence of dissipation mechanisms. The conservation equations of the reacting system are given by

$$\frac{\partial \rho}{\partial t} + \nabla \cdot (\rho \mathbf{u}) = 0, \tag{12a}$$

$$\frac{\partial \mathbf{u}}{\partial t} + \mathbf{u} \cdot \nabla \mathbf{u} + \frac{1}{\rho} \nabla p = 0, \tag{12b}$$

$$\frac{\partial p}{\partial t} + \mathbf{u} \cdot \nabla p + \gamma p \nabla \cdot \mathbf{u} = K q_0 (\gamma - 1)\, \rho z\, e^{-E_a/T}, \tag{12c}$$

$$\frac{\partial z}{\partial t} + \mathbf{u} \cdot \nabla z = -K z\, e^{-E_a/T}. \tag{12d}$$

The equation of state of the reacting system is

$$T = \frac{p}{\rho}. \tag{13}$$

In the equations above, $\mathbf{u} = (u, v)$ is the velocity vector, T is the gas temperature normalized by the gas constant, and z is the reactant mass fraction, satisfying $0 \leq z \leq 1$. The parameters of the system are

- γ, the specific heat ratio, assumed common for both species,
- q_0, the heat-release parameter,
- E_a, the activation-energy parameter, and
- K, a scaling factor.

In the system under consideration, there are five dependent unknowns, therefore $M = 5$, on a three-dimensional space-time, therefore $N = 2$.

Assume that the solution is continuous and consider an arbitrary but fixed spatial unit vector, $\mathbf{n} = (n_1, n_2)$. Then, for the system above, the characteristic polynomial gives

$$(\mathbf{u} \cdot \mathbf{n} - \lambda)^3 \left((\mathbf{u} \cdot \mathbf{n} - \lambda)^2 - (a\, |\mathbf{n}|)^2 \right) = 0, \tag{14}$$

where

$$a = \sqrt{\frac{\gamma p}{\rho}}. \tag{15}$$

This quantity is usually referred to as the frozen speed of sound. Relation (14) yields, in view of (8),

$$\left(\frac{\partial \phi_N}{\partial t} + \mathbf{u} \cdot \nabla \phi_N \right)^3 \left(\left(\frac{\partial \phi_N}{\partial t} + \mathbf{u} \cdot \nabla \phi_N \right)^2 - (a\, |\nabla \phi_N|)^2 \right) = 0. \tag{16}$$

The convective manifold defined by the equation

$$\frac{\partial \phi_N}{\partial t} + \mathbf{u} \cdot \nabla \phi_N = 0 \tag{17}$$

has a three-fold degeneracy. The associated triple eigenvalue is $\lambda_{1,2,3} = \mathbf{u} \cdot \mathbf{n}$. The acoustic manifold defined by the equation

$$\frac{\partial \phi_N}{\partial t} + \mathbf{u} \cdot \nabla \phi_N + a \, |\nabla \phi_N| = 0 \tag{18}$$

corresponds to the eigenvalue $\lambda_4 = \mathbf{u} \cdot \mathbf{n} - a$, while the acoustic manifold defined by the equation

$$\frac{\partial \phi_N}{\partial t} + \mathbf{u} \cdot \nabla \phi_N - a \, |\nabla \phi_N| = 0 \tag{19}$$

corresponds to the eigenvalue $\lambda_5 = \mathbf{u} \cdot \mathbf{n} + a$. The left eigenvectors of the system are, respectively,

$$\mathbf{l}_1 = \left[0, \, -\frac{n_2}{n_1}, \, 1, \, 0, \, 0\right], \tag{20a}$$

$$\mathbf{l}_2 = \left[-a^2, \, 0, \, 0, \, 1, \, 0\right], \tag{20b}$$

$$\mathbf{l}_3 = [0, \, 0, \, 0, \, 0, \, 1], \tag{20c}$$

$$\mathbf{l}_4 = [0, \, n_1 \rho a, \, n_2 \rho a, \, 1, \, 0], \tag{20d}$$

$$\mathbf{l}_5 = [0, \, -n_1 \rho a, \, -n_2 \rho a, \, 1, \, 0]. \tag{20e}$$

Applying (10), the original system of equations can be written in characteristic form,

$$\frac{\partial}{\partial t} \log\left(p \rho^{-\gamma}\right) + \mathbf{u} \cdot \nabla \left(\log\left(p \rho^{-\gamma}\right)\right) = K \, (\gamma - 1) \, q_0 \, \rho \, \frac{z}{T} \, e^{-E_a/T}, \tag{21a}$$

$$\frac{\partial z}{\partial t} + \mathbf{u} \cdot \nabla z = -K \, z \, e^{-E_a/T}, \tag{21b}$$

$$\frac{\partial}{\partial t}\left(\mathbf{u} \cdot \mathbf{n}^{\perp}\right) + \mathbf{u} \cdot \nabla \left(\mathbf{u} \cdot \mathbf{n}^{\perp}\right) = -\frac{1}{\rho} \nabla p \cdot \mathbf{n}^{\perp}, \tag{21c}$$

$$\left(\frac{\partial p}{\partial t} + \rho a \, \mathbf{n} \cdot \frac{\partial \mathbf{u}}{\partial t}\right) + (\mathbf{u} + a\mathbf{n}) \cdot (\nabla p + \rho a \, \mathbf{n} \cdot \nabla \mathbf{u}) = R, \tag{21d}$$

$$\left(\frac{\partial p}{\partial t} - \rho a \, \mathbf{n} \cdot \frac{\partial \mathbf{u}}{\partial t}\right) + (\mathbf{u} - a\mathbf{n}) \cdot (\nabla p - \rho a \, \mathbf{n} \cdot \nabla \mathbf{u}) = R, \tag{21e}$$

where

$$R = \rho a^2 \left[\mathbf{n} \cdot (\nabla \mathbf{u}) \, \mathbf{n} - \nabla \cdot \mathbf{u}\right] + K \, (\gamma - 1) \, q_0 \, \rho \, z \, e^{-E_a/T}. \tag{22}$$

In the equations above, $\mathbf{n}^{\perp}$ stands for the spatial unit vector normal to $\mathbf{n}$. The first three equations hold along the fluid stream-lines, while the fourth and fifth equations hold along the bicharacteristics.

The terms on the right-hand side of equations (21) act as forcing terms and do not allow a straightforward extension of the method of characteristics, as used for the one-dimensional Euler equations of gas dynamics. The splitting approach in the design of shock-capturing schemes, with or without source terms, is to fix $\mathbf{n}$ parallel to the grid direction, ignore the velocity component normal to $\mathbf{n}$ and the terms on the right-hand side of the characteristic equations (21), and finally solve for the remaining parts of the equations along the one-dimensional characteristic directions. By employing this strategy, however, one disregards information that is coming from other flow directions.

The idea behind the present design of unsplit, multidimensional schemes is to find manifolds in space-time along which the equivalent one-dimensional, homogeneous characteristic equations

hold. The immediate advantage of using such manifolds is that these equations can be easily discretized and solved numerically. Assume that the solution vector is continuous up to first-order derivatives. Then, the convective velocities $\mathbf{u}_0$, $\mathbf{u}_\mathrm{r}$, $\mathbf{u}_\perp$, $\mathbf{u}_+$, $\mathbf{u}_-$ can be defined so that the following relations are satisfied:

$$\mathbf{u}_0 \cdot \nabla \log\left(p\rho^{-\gamma}\right) = -K\left(\gamma - 1\right) q_0 \frac{z}{T} e^{-E_\mathrm{a}/T}, \tag{23a}$$

$$\mathbf{u}_\mathrm{r} \cdot \nabla z = K\, z\, e^{-E_\mathrm{a}/T}, \tag{23b}$$

$$\mathbf{u}_\perp \cdot \nabla\left(\mathbf{u} \cdot \mathbf{n}^\perp\right) = \frac{1}{\rho} \nabla p \cdot \mathbf{n}^\perp, \tag{23c}$$

$$\mathbf{u}_+ \cdot \left(\nabla p + \rho\, a\, \mathbf{n} \cdot \nabla \mathbf{u}\right) = -R, \tag{23d}$$

$$\mathbf{u}_- \cdot \left(\nabla p - \rho\, a\, \mathbf{n} \cdot \nabla \mathbf{u}\right) = -R. \tag{23e}$$

Additionally, consider the manifolds $\mathcal{S}_0$, $\mathcal{S}_+$, $\mathcal{S}_-$, $\mathcal{S}_\mathrm{r}$, $\mathcal{S}_\perp$, defined as the integral surfaces of the following equations:

$$\mathcal{S}_0 : \frac{D}{Dt} \log(p\rho^{-\gamma}) = 0, \tag{24a}$$

$$\mathcal{S}_\mathrm{r} : \frac{Dz}{Dt} = 0, \tag{24b}$$

$$\mathcal{S}_\perp : \frac{D}{Dt}\left(\mathbf{u} \cdot \mathbf{n}^\perp\right) = 0, \tag{24c}$$

$$\mathcal{S}_+ : \frac{Dp}{Dt} + \rho a \frac{D}{Dt}(\mathbf{u} \cdot \mathbf{n}) = 0, \tag{24d}$$

$$\mathcal{S}_- : \frac{Dp}{Dt} - \rho a \frac{D}{Dt}(\mathbf{u} \cdot \mathbf{n}) = 0. \tag{24e}$$

Combining relations (23) and (21), it can be verified that the integral curves of the following vector fields lie on the manifolds (24):

$$\left\{(t, \mathbf{x}) \in t \times \Re^2 : \frac{\mathrm{d}\mathbf{x}}{\mathrm{d}t} = \mathbf{u} + \mathbf{u}_0\right\} \in \mathcal{S}_0, \tag{25a}$$

$$\left\{(t, \mathbf{x}) \in t \times \Re^2 : \frac{\mathrm{d}\mathbf{x}}{\mathrm{d}t} = \mathbf{u} + \mathbf{u}_\mathrm{r}\right\} \in \mathcal{S}_\mathrm{r}, \tag{25b}$$

$$\left\{(t, \mathbf{x}) \in t \times \Re^2 : \frac{\mathrm{d}\mathbf{x}}{\mathrm{d}t} = \mathbf{u} + \mathbf{u}_\perp\right\} \in \mathcal{S}_\perp, \tag{25c}$$

$$\left\{(t, \mathbf{x}) \in t \times \Re^2 : \frac{\mathrm{d}\mathbf{x}}{\mathrm{d}t} = \mathbf{u} + a\,\mathbf{n} + \mathbf{u}_+\right\} \in \mathcal{S}_+, \tag{25d}$$

$$\left\{(t, \mathbf{x}) \in t \times \Re^2 : \frac{\mathrm{d}\mathbf{x}}{\mathrm{d}t} = \mathbf{u} - a\,\mathbf{n} + \mathbf{u}_-\right\} \in \mathcal{S}_-. \tag{25e}$$

The convective velocities $\mathbf{u}_0$, $\mathbf{u}_\mathrm{r}$, $\mathbf{u}_\perp$, $\mathbf{u}_+$, $\mathbf{u}_-$ depend locally on the spatial gradients of the flow and are defined through the inner-product relations (23). These relations must be regarded as the necessary compatibility conditions for the integral curves given by (25) to lie on the corresponding manifolds. Each of these equations is linear in the components of the corresponding convective velocity. This is because each of the ODEs (24) holds on a family of curves that constitutes a two-dimensional manifold on the three-dimensional Euclidean space-time. Every curve on this manifold passing through a point P corresponds to a different choice of convective velocity, see Figure 1.

The definition of these manifolds is of local character because it is made under the assumption of a smooth solution vector. The existence of discontinuities in the solution or its derivatives does

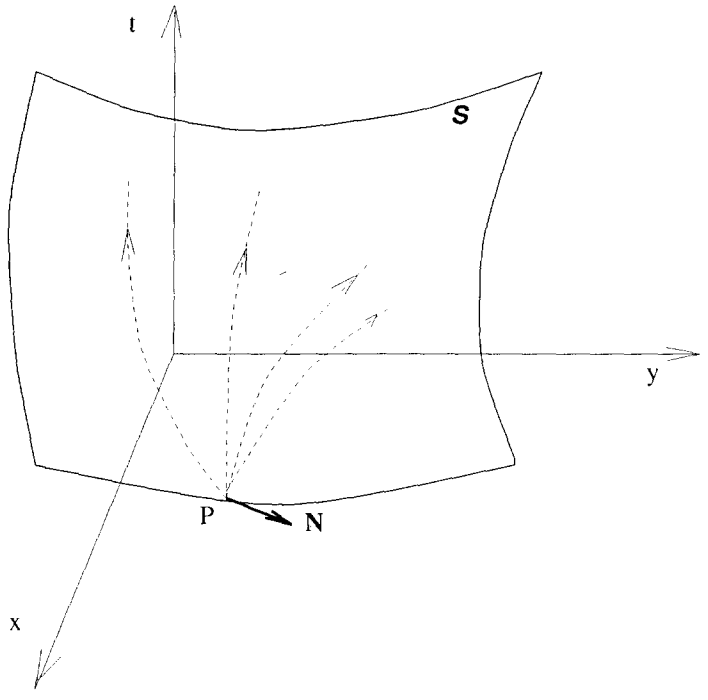

Figure 1. A Riemann invariant manifold in the three-dimensional Euclidean space-time.

not allow construction of the five manifolds, globally. This is not, however, a serious restriction for numerical purposes. If a discontinuity is present in the flow-field, each of these manifolds can be defined, and used in the computations, on either side of the discontinuity. The presence of shocks, for example, is accommodated by supplementing the equations that hold on the manifolds, with the appropriate jump conditions across the discontinuities. In other words, an appropriate Riemann problem has to be solved. In this case, care must be taken so that not both initial states are taken from the unshocked region, because then the information carried by the manifolds will not propagate through the approaching shock. This shock-capturing strategy is equivalent to the one used in traditional schemes which trace the bicharacteristic rays on each side of the discontinuity.

Some numerically useful choices of directions on the manifolds of interest are presented below. First, consider the invariant manifold $\mathcal{S}_+$. Let $\mathbf{N}_+$ denote the spatial unit vector normal to this front. Then one gets

$$\mathbf{N}_+ = \frac{\nabla p + \rho a \nabla(\mathbf{u}\cdot\mathbf{n})}{|\nabla p + \rho a \nabla(\mathbf{u}\cdot\mathbf{n})|}. \tag{26}$$

$\mathbf{N}_+$ depends on the spatial unit vector $\mathbf{n}$. Actually, there is a family of manifolds $\mathcal{S}_+$, each manifold corresponding to a different choice of $\mathbf{n}$. The unit vector $\mathbf{n}$, which is assumed to be arbitrary but fixed, acts as a "label" for the particular manifold under consideration. In other words, $\mathbf{n}$ is the free parameter of the one-parameter family of manifolds $\mathcal{S}_+$. This is also true for the family of manifolds $\mathcal{S}_-$ and $\mathcal{S}_\perp$. It is not true, however, for $\mathcal{S}_0$ and $\mathcal{S}_r$ because the orientation of these manifolds does not depend on $\mathbf{n}$, see equations (25).

Furthermore, $\mathbf{n}$ gives the spatial direction along which a one-dimensional characteristic problem holds. By keeping $\mathbf{u}_+$ fixed and letting $\mathbf{n}$ rotate a full circle, one gets a conoid of invariant curves passing through the point P. An example of the relative position of this conoid with respect to the conoid that is formed by rotation of the bicharacteristics (ray conoid) is sketched in Figure 2.

The velocity of the front $\mathcal{S}_+$ is given by

$$\mathbf{c}_+ = \mathbf{u} + a\,\mathbf{n} + \mathbf{u}_+. \tag{27}$$

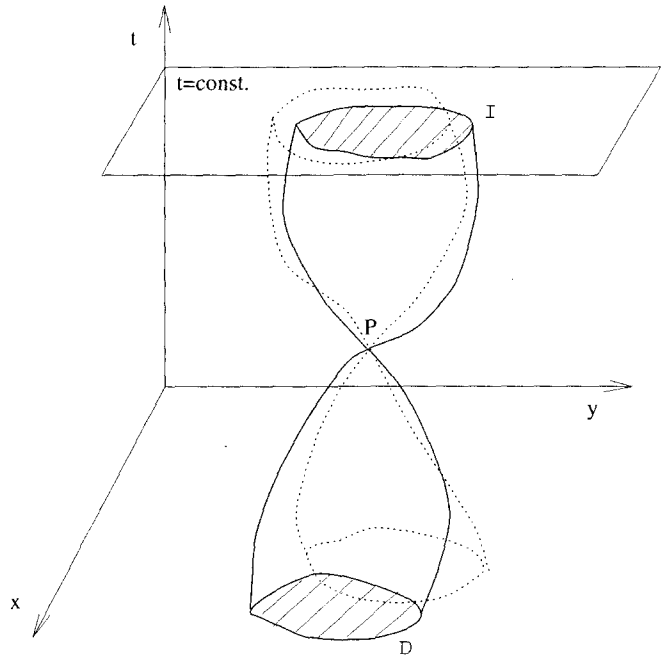

Figure 2. Relative position of the invariant conoid (solid line) formed by the rotation of **n**, with respect the ray conoid (dotted line) passing through a point P in space-time.

A useful choice for $\mathbf{u}_+$ is to seek $|\mathbf{u}_+|_{\min}$. The curve on $\mathcal{S}_+$ that corresponds to this choice is the curve that lies as close to the equivalent bicharacteristic ray as possible. This means that among all intersection points of $\mathcal{S}_+$ and the constant-t plane, the one that belongs to the above curve is the closest to the intersection of the bicharacteristic ray and the constant-t plane. Then $\mathbf{u}_+ \parallel \mathbf{N}_+$, and in fact,

$$\mathbf{u}_+ = \left(\frac{-R}{|\nabla p + \rho a \nabla(\mathbf{u}\cdot\mathbf{n})|} \right) \mathbf{N}_+. \tag{28}$$

The velocity of the front $\mathcal{S}_+$ can be written as

$$\mathbf{c}_+ = \mathbf{u} + aM_+ \mathbf{N}_+. \tag{29}$$

In the equation above, the expression for M_+ can be obtained from (28) and (27). The result is

$$M_+ = \mathbf{n}\cdot\mathbf{N}_+ - \frac{R}{a\,|\nabla p + \rho a \nabla(\mathbf{u}\cdot\mathbf{n})|}. \tag{30}$$

The dimensionless parameter M_+ is a measure of the deviation of the surface element around the selected curve on the manifold $\mathcal{S}_+$ from the bicharacteristic ray $\mathbf{u} + a\mathbf{n}$. When $|M_+| < 1$, the surface element is time-like. When $|M_+| > 1$, the surface element is space-like (and when $|M_+| = 1$, it is characteristic). When the surface element of $\mathcal{S}_+$ is space-like, it lies outside the domain of dependence of a given point P. This might appear counter-intuitive but it has to do with the fact that knowledge of the local spatial gradients of the flow and their smoothness constitutes additional information about how the initial data are related. This information can propagate with speeds greater than the characteristic speeds, as (30) reveals, and can be used for computational purposes, see also relative discussion in [10].

The information about $\mathcal{S}_+$ is contained in $\mathbf{N}_+$ and M_+. These quantities provide the direction of this manifold and its relative position with respect to the characteristic manifolds. Both of these quantities depend directly on the spatial unit vector **n**. This dependence is due to the

multidimensional character of the problem under consideration. The intersection of a manifold in space-time and the local characteristic ray cone can be examined by considering the projection vector, $\mathbf{V}_p$, of an arbitrary bicharacteristic direction $\hat{\mathbf{n}}$,

$$\mathbf{V}_p = \mathbf{u} + a\hat{\mathbf{n}}, \tag{31}$$

on the manifold of interest. For the case of $\mathcal{S}_+$, one can readily find that the projection of a curve $\dot{\mathbf{x}}(t) = \mathbf{W}$ on $\mathcal{S}_+$ is the curve $\dot{\mathbf{x}}(t) = \mathbf{w}_p$ such that the norm $|\mathbf{W} - \mathbf{w}_p|$ attains a minimum. This occurs if

$$(\mathbf{W} - \mathbf{w}_p) \parallel \mathbf{N}_+.$$

When this condition is satisfied, then $\mathbf{W} = \mathbf{V}_p$ and $\mathbf{w}_p = \mathbf{c}_+$. Furthermore, one gets that

$$(\mathbf{W} - \mathbf{w}_p) = \mathbf{V}_p - \mathbf{c}_+ = a\,(\hat{\mathbf{n}} \cdot \mathbf{N}_+ - M_+)\,\mathbf{N}_+. \tag{32}$$

The bicharacteristic ray lies locally on the invariant manifold $\mathcal{S}_+$ if the right-hand side of the above expression becomes zero, i.e., if the following relation is satisfied:

$$M_+ = \hat{\mathbf{n}} \cdot \mathbf{N}_+. \tag{33}$$

This equation admits a solution only if $|M_+| \leq 1$. Since both $\mathbf{N}_+$ and $\hat{\mathbf{n}}$ are unit vectors, this condition is satisfied when the surface element of $\mathcal{S}_+$ lies within the characteristic ray cone. This implies that whenever the invariant manifold $\mathcal{S}_+$ is not space-like, there are bicharacteristic directions along which an equivalent one-dimensional problem holds.

Similar relations hold for the invariant manifold $\mathcal{S}_-$. The spatial unit normal to this front is given by

$$\mathbf{N}_- = \frac{\nabla p - \rho a \nabla(\mathbf{u} \cdot \mathbf{n})}{|\nabla p - \rho a \nabla(\mathbf{u} \cdot \mathbf{n})|}, \tag{34}$$

and the velocity of this front is given by

$$\mathbf{c}_- = \mathbf{u} - a\,\mathbf{n} + \mathbf{u}_-.$$

Along the curve of $\mathcal{S}_-$ that lies as close as possible to the equivalent bicharacteristic, the norm $|\mathbf{n}_-|$ attains a minimum. In this case, $\mathbf{u}_- \parallel \mathbf{N}_-$, and one gets

$$\mathbf{u}_- = \left(\frac{-R}{|\nabla p - \rho a \nabla(\mathbf{u} \cdot \mathbf{n})|}\right) \mathbf{N}_-. \tag{35}$$

The velocity of the front $\mathcal{S}_+$ can be written as

$$\mathbf{c}_- = \mathbf{u} - aM_-\,\mathbf{N}_-. \tag{36}$$

M_- is the dimensionless parameter that measures the deviation of the curve from the bicharacteristic $\mathbf{u} - a\mathbf{n}$. It is defined as

$$M_- = \mathbf{n} \cdot \mathbf{N}_- + \frac{R}{a\,|\nabla p - \rho a \nabla(\mathbf{u} \cdot \mathbf{n})|}. \tag{37}$$

As in the case of $\mathcal{S}_+$, a surface element on $\mathcal{S}_-$ is time-like, characteristic, or space-like, according to whether $|M_-| < 1$, $|M_-| = 1$, or $|M_-| > 1$, respectively. Using arguments similar to the ones employed when $\mathcal{S}_+$ was examined, one can find that the necessary condition for a characteristic curve to lie on $\mathcal{S}_-$ is

$$M_- = \hat{\mathbf{n}} \cdot \mathbf{N}_-. \tag{38}$$

It remains to investigate the structure of the invariant manifolds $\mathcal{S}_0, \mathcal{S}_\mathrm{r}, \mathcal{S}_\perp$ and determine the curves along these manifolds that can be used for numerical purposes. The spatial unit normal vectors of these manifolds are given by

$$\mathbf{N}_0 = \frac{\nabla p - a^2 \nabla \rho}{|\nabla p - a^2 \nabla \rho|}, \tag{39a}$$

$$\mathbf{N}_\mathrm{r} = \frac{\nabla z}{|\nabla z|}, \tag{39b}$$

$$\mathbf{N}_\perp = \frac{\nabla \left(\mathbf{u} \cdot \mathbf{n}^\perp \right)}{|\nabla \left(\mathbf{u} \cdot \mathbf{n}^\perp \right)|}, \tag{39c}$$

respectively. The corresponding front velocities are

$$\mathbf{c}_0 = \mathbf{u} + \mathbf{u}_0, \tag{40a}$$

$$\mathbf{c}_\mathrm{r} = \mathbf{u} + \mathbf{u}_\mathrm{r}, \tag{40b}$$

$$\mathbf{c}_\perp = \mathbf{u} + \mathbf{u}_\perp. \tag{40c}$$

As mentioned earlier, the convective velocities $\mathbf{u}_0$, $\mathbf{u}_\mathrm{r}$, and $\mathbf{u}_\perp$ need only satisfy the compatibility conditions (23). Since all of these conditions are linear equations in the velocity space, a particular choice of a convective velocity represents a curve along the corresponding manifold. It is natural to select the velocities whose norm attain a minimum, i.e., to look for $|\mathbf{u}_0|_\mathrm{min}$, $|\mathbf{u}_\mathrm{r}|_\mathrm{min}$, $|\mathbf{u}_\perp|_\mathrm{min}$. Then, one immediately gets

$$\mathbf{u}_0 \parallel \mathbf{N}_0, \tag{41a}$$

$$\mathbf{u}_\mathrm{r} \parallel \mathbf{N}_\mathrm{r}, \tag{41b}$$

$$\mathbf{u}_\perp \parallel \mathbf{N}_\perp. \tag{41c}$$

Using relation (39), the following expressions are deduced:

$$\mathbf{u}_0 = -\frac{K\,(\gamma - 1)\,q_0\,\rho\,z\,e^{-E_\mathrm{a}/T}}{|\nabla p - a^2 \nabla \rho|}\,\mathbf{N}_0, \tag{42a}$$

$$\mathbf{u}_\mathrm{r} = \frac{K\,z\,e^{-E_\mathrm{a}/T}}{|\nabla z|}\,\mathbf{N}_\mathrm{r}, \tag{42b}$$

$$\mathbf{u}_\perp = \frac{\nabla p \cdot \mathbf{n}^\perp}{\rho\,|\nabla (\mathbf{u} \cdot \mathbf{n}^\perp)|}\,\mathbf{N}_\perp. \tag{42c}$$

Alternatively, one can introduce dimensionless parameters,

$$M_0 \equiv \frac{K\,(\gamma - 1)\,q_0\,z\,e^{-E_\mathrm{a}/T}}{a\,|\nabla p - a^2 \nabla \rho|}, \tag{43a}$$

$$M_\mathrm{r} \equiv \frac{K\,z\,e^{-E_\mathrm{a}/T}}{a\,|\nabla z|}, \tag{43b}$$

$$M_\perp \equiv \frac{\nabla p \cdot \mathbf{n}^\perp}{\rho\,a\,|\nabla \left(\mathbf{u} \cdot \mathbf{n}^\perp \right)|}, \tag{43c}$$

and express the convective velocities in the following fashion:

$$\mathbf{u}_0 = -aM_0\mathbf{N}_0, \tag{44a}$$

$$\mathbf{u}_\mathrm{r} = aM_\mathrm{r}\mathbf{N}_\mathrm{r}, \tag{44b}$$

$$\mathbf{u}_\perp = aM_\perp\mathbf{N}_\perp. \tag{44c}$$

As in the case with M_+ and M_-, the parameters M_0, M_r, and $M_\perp$, determine the relative position of the corresponding invariant manifolds, $\mathcal{S}_0$, $\mathcal{S}_r$, and $\mathcal{S}_\perp$, with respect to the local ray cone. If a parameter is greater than unity, then its corresponding manifold is space-like and it is time-like otherwise.

The intersection of $\mathcal{S}_0$, $\mathcal{S}_r$, and $\mathcal{S}_\perp$ with the ray cone can be examined in the same way as above, i.e., by considering the projection vector of an arbitrary characteristic direction. Then, one deduces that the following condition has to be satisfied for a characteristic curve to lie on $\mathcal{S}_0$:

$$M_0 = \hat{\mathbf{n}} \cdot \mathbf{N}_0. \tag{45}$$

Similarly, if a characteristic curve is to lie on $\mathcal{S}_r$, then the necessary condition is

$$M_r = \hat{\mathbf{n}} \cdot \mathbf{N}_r. \tag{46}$$

Finally, if a characteristic curve is to lie on $\mathcal{S}_\perp$, then the necessary condition is

$$M_\perp = \hat{\mathbf{n}} \cdot \mathbf{N}_\perp. \tag{47}$$

2.1. Description of the Numerical Scheme

The compressible Euler equations for reacting flows (12), written in integral form, are

$$\frac{\mathrm{d}}{\mathrm{d}t}\int_V \rho \, \mathrm{d}V + \int_S \rho \, \mathbf{u} \cdot \mathrm{d}\mathbf{S} = 0, \tag{48a}$$

$$\frac{\mathrm{d}}{\mathrm{d}t}\int_V \rho\mathbf{u} \, \mathrm{d}V + \int_S \rho\mathbf{u} \, \mathbf{u} \cdot \mathrm{d}\mathbf{S} + \int_S p \, \mathrm{d}\mathbf{S} = 0, \tag{48b}$$

$$\frac{\mathrm{d}}{\mathrm{d}t}\int_V \rho e_t \, \mathrm{d}V + \int_S \rho e_t \, \mathbf{u} \cdot \mathrm{d}\mathbf{S} + \int_S p\mathbf{u} \cdot \mathrm{d}\mathbf{S} = 0, \tag{48c}$$

$$\frac{\mathrm{d}}{\mathrm{d}t}\int_V \rho z \, \mathrm{d}V + \int_S \rho z \, \mathbf{u} \cdot \mathrm{d}\mathbf{S} - \int_V \rho \, g(T,z) \, \mathrm{d}V = 0,$$

where e_t is the total specific energy,

$$e_t = \frac{p}{\rho(\gamma - 1)} + q_0 z + \frac{u^2}{2}, \tag{49}$$

and $g(T,z)$ is the source term of the reaction equation,

$$g(T,z) = -K z e^{-E_a/T}. \tag{50}$$

These equations are written for an arbitrary control volume V whose boundary S has zero velocity. The procedure of discretization and numerical evaluation of these integrals at each computational cell is given below. The resulting algorithm is second-order accurate for smooth parts of the flow.

Consider a simply-connected domain consisting of $N_c \times M_c$ quadrilateral cells of arbitrary shape. The area of the (i,j) cell is denoted by $\Delta S_{i,j}$, and the coordinates of the center of the cell are denoted by $(x^c_{i,j}, y^c_{i,j})$. The interface between the cells (i,j) and $(i+1,j)$ is denoted by $(i+1/2,j)$. Similarly, the interface between the cells (i,j) and $(i,j+1)$ is denoted by $(i,j+1/2)$. Finally, the unit vector normal to a cell interface is denoted by $\mathbf{n}_s$, and the length of a cell interface is denoted by l.

Bilinear variation of all variables is assumed in each cell. The generic quantity q is then given by

$$q(i,j) = q_{i,j} + (q_x)_{i,j}\left(x - x^c_{i,j}\right) + (q_y)_{i,j}\left(y - y^c_{i,j}\right), \qquad i = 1,\ldots,N_c, \quad j = 1,\ldots,M_c, \tag{51}$$

where $q_{i,j}$, the average value of q in the (i,j) cell and $(q_x)_{i,j}, (q_y)_{i,j}$ are the slopes of q inside this cell.

Under the assumption of bilinear variation of q, the slopes are constant. Then, $q_{i,j}$ is just the value of q at the center of the cell. The slopes $(q_x)_{i,j}, (q_y)_{i,j}$ are evaluated through the divergence theorem. For bilinear functions, this theorem takes the form,

$$[(q_x)_{i,j}, (q_y)_{i,j}]\,\Delta S_{i,j} = (q\mathbf{n}_s\, l)_{i\pm 1/2,j} + (q\mathbf{n}_s\, l)_{i,j\pm 1/2}. \tag{52}$$

In the relation above, q must be evaluated at the center of each cell interface. This is performed with the following procedure.

Assume that q is to be computed at the center of the left interface, and let Δl_i denote the distance between $(x^c_{i,j}, y^c_{i,j})$ and $(x^c_{i-1,j}, y^c_{i-1,j})$. Consider the left divided difference

$$\Delta q_{\mathrm{L}} \equiv \frac{q_{i,j} - q_{i-1,j}}{\Delta l_i}. \tag{53}$$

The differences $\Delta q_{\mathrm{R}}, \Delta q_{\mathrm{U}}, \Delta q_{\mathrm{D}}$, in the right, up, and down directions, respectively, are defined in a similar fashion. Then, the value of q at the left interface is given by

$$q_{i-1/2,j} = q_{i,j} - 0.5\,\Delta l_i\,\Delta q_{\mathrm{LR}},$$

where Δq_{LR} is an approximation of the slope of q in the direction normal to the cell interface. It can be computed from Δq_{L} and Δq_{R} with the use of van Albada's limiter, [12],

$$\Delta q_{\mathrm{LR}} = \mathrm{ave}(\Delta q_{\mathrm{L}}, \Delta q_{\mathrm{R}}) \tag{54}$$

and

$$\mathrm{ave}(a,b) \equiv \frac{a+b}{2}\left(1 - \frac{(a-b)^2}{a^2+b^2+\epsilon^2}\right), \tag{55}$$

with ϵ being a small positive number, say, $\epsilon = 10^{-12}$. This slope-limiting procedure is employed to preserve the monotonicity of q near discontinuities while maintaining second-order accuracy in both space and time for smooth parts of the flow. The evaluation of q at the centers of the other cell interfaces is performed by repeating these steps to the appropriate interface.

For the numerical solution of the system of conservation equations, mass-averaged values of the conservative variables are considered,

$$m_{i,j} \equiv \int_{(i,j)} \rho\,\mathrm{d}x\,\mathrm{d}y, \tag{56a}$$

$$m_{i,j}u_{i,j} \equiv \int_{(i,j)} \rho u\,\mathrm{d}x\,\mathrm{d}y, \tag{56b}$$

$$m_{i,j}v_{i,j} \equiv \int_{(i,j)} \rho v\,\mathrm{d}x\,\mathrm{d}y, \tag{56c}$$

$$m_{i,j}e_{\mathrm{t}i,j} \equiv \int_{(i,j)} \rho e_t\,\mathrm{d}x\,\mathrm{d}y, \tag{56d}$$

$$m_{i,j}z_{i,j} \equiv \int_{(i,j)} \rho\, z\,\mathrm{d}x\,\mathrm{d}y. \tag{56e}$$

For the source term, set

$$m_{i,j}g_{i,j} \equiv \int_{(i,j)} \rho g(T,z)\,\mathrm{d}x\,\mathrm{d}y. \tag{57}$$

The flux vectors are given by

$$\mathbf{F}_m \equiv [\rho u,\ \rho v]\,, \tag{58a}$$

$$\mathbf{F}_u \equiv \left[\rho u^2 + p,\ \rho u\right], \tag{58b}$$

$$\mathbf{F}_v \equiv \left[\rho uv,\ \rho v^2 + p\right], \tag{58c}$$

$$\mathbf{F}_e \equiv [\rho e_t u + pu,\ \rho e_t v + pv]\,, \tag{58d}$$

$$\mathbf{F}_z \equiv [\rho\, zu,\ \rho\, zv]\,. \tag{58e}$$

The integration of the flux vectors along each cell interface is performed using the midpoint rule.

Consequently, the proposed numerical scheme, which evaluates the solution at time $(n+1)\Delta t$ from the solution at the previous time $n\Delta t$, can be written as

$$\begin{aligned}(m_{i,j})^{n+1} = (m_{i,j})^n &- \Delta t\left[(l\mathbf{n}_s\cdot\mathbf{F}_m)^{n+1/2}_{i+1/2,j} - (l\mathbf{n}_s\cdot\mathbf{F}_m)^{n+1/2}_{i-1/2,j}\right]\\ &-\Delta t\left[(l\mathbf{n}_s\cdot\mathbf{F}_m)^{n+1/2}_{i,j+1/2} - (l\mathbf{n}_s\cdot\mathbf{F}_m)^{n+1/2}_{i,j-1/2}\right],\end{aligned} \tag{59a}$$

$$\begin{aligned}(m_{i,j}u_{i,j})^{n+1} = (m_{i,j}u_{i,j})^n &- \Delta t\left[(l\mathbf{n}_s\cdot\mathbf{F}_u)^{n+1/2}_{i+1/2,j} - (l\mathbf{n}_s\cdot\mathbf{F}_u)^{n+1/2}_{i-1/2,j}\right]\\ &-\Delta t\left[(l\mathbf{n}_s\cdot\mathbf{F}_u)^{n+1/2}_{i,j+1/2} - (l\mathbf{n}_s\cdot\mathbf{F}_u)^{n+1/2}_{i,j-1/2}\right],\end{aligned} \tag{59b}$$

$$\begin{aligned}(m_{i,j}v_{i,j})^{n+1} = (m_{i,j}v_{i,j})^n &- \Delta t\left[(l\mathbf{n}_s\cdot\mathbf{F}_v)^{n+1/2}_{i+1/2,j} - (l\mathbf{n}_s\cdot\mathbf{F}_v)^{n+1/2}_{i-1/2,j}\right]\\ &-\Delta t\left[(l\mathbf{n}_s\cdot\mathbf{F}_v)^{n+1/2}_{i,j+1/2} - (l\mathbf{n}_s\cdot\mathbf{F}_v)^{n+1/2}_{i,j-1/2}\right],\end{aligned} \tag{59c}$$

$$\begin{aligned}(m_{i,j}e_{i,j})^{n+1} = (m_{i,j}e_{i,j})^n &- \Delta t\left[(l\mathbf{n}_s\cdot\mathbf{F}_e)^{n+1/2}_{i+1/2,j} - (l\mathbf{n}_s\cdot\mathbf{F}_e)^{n+1/2}_{i-1/2,j}\right]\\ &-\Delta t\left[(l\mathbf{n}_s\cdot\mathbf{F}_e)^{n+1/2}_{i,j+1/2} - (l\mathbf{n}_s\cdot\mathbf{F}_e)^{n+1/2}_{i,j-1/2}\right],\end{aligned} \tag{59d}$$

$$\begin{aligned}(m_{i,j}z_{i,j})^{n+1} = (m_{i,j}z_{i,j})^n &- \Delta t\left[(l\mathbf{n}_s\cdot\mathbf{F}_z)^{n+1/2}_{i+1/2,j} - (l\mathbf{n}_s\cdot\mathbf{F}_z)^{n+1/2}_{i-1/2,j}\right]\\ -\Delta t\left[(l\mathbf{n}_s\cdot\mathbf{F}_z)^{n+1/2}_{i,j+1/2} - (l\mathbf{n}_s\cdot\mathbf{F}_z)^{n+1/2}_{i,j-1/2}\right] &+ \Delta t\Delta S_{i,j}\,(m_{i,j}g_{i,j})^{n+1/2}.\end{aligned} \tag{59e}$$

The flux terms in relation above have to be evaluated at the center of each cell interface, and at time $t = (n+1/2)\Delta t$. This is performed by using the information provided by the Riemann invariant manifolds that were described in the previous section. This procedure is illustrated below for the interface between the cells (i,j) and $(i+1,j)$. For the other three cell interfaces, the procedure is exactly the same.

Let $\mathbf{x}_w = (x_w, y_w)$ denote the center of this interface. One has to trace specific curves along the five invariant manifolds that pass through the point with coordinates $(x_w, y_w, (n+1/2)\Delta t)$ and find the intersection of these curves with the surface $t = n\Delta t$. Then, the equations that hold on the manifolds have to be discretized and solved numerically.

But first, one must select $\mathbf{n}$. Recall that there is a one-parameter family of the manifolds $\mathcal{S}_+$ that is generated by the rotation of $\mathbf{n}$. These manifolds form a conoid equivalent to the ray conoid. By selecting $\mathbf{n}$, one essentially decides the direction along which the ODEs that hold on $\mathcal{S}_+$ and $\mathcal{S}_-$ are solved. Numerical experiments showed that selecting the unit normal to the cell interface, i.e., $\mathbf{n} = \mathbf{n}_s$, works well in practice.

Having determined the manifold $\mathcal{S}_+$ that will be used, one has to decide which specific curve on $\mathcal{S}_+$ should be traced forward in time, i.e., which convective velocity $\mathbf{u}_+$ will be used. The intersection of $\mathcal{S}_+$ with the plane $t = n\Delta t$ is the locus of the points that are connected with the point $(x_w, y_w, (n+1/2)\Delta t)$ by the characteristic differential equation (24d), see Figure 3. Each point of this curve corresponds to a specific $\mathbf{u}_+$. In the present work, the convective velocity $\mathbf{u}_+$

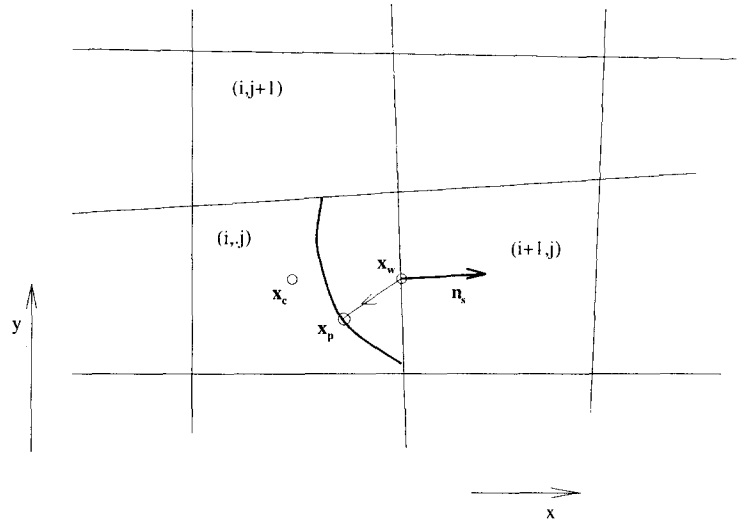

Figure 3. The locus of the points at $t = n\Delta t$ that are connected with (x_w, y_w) through (24d).

has been selected to satisfy equation (28). In other words, the curve that lies as close to the equivalent bicharacteristic as possible has been chosen.

The coordinates of the point at which this curve intersects the plane $t = n\Delta t$, say $\mathbf{x}_p$, are evaluated by solving equation (25d) numerically. For this purpose, the selected curve is approximated by a straight line. After some straightforward calculations, one gets the following expression for the coordinates of $\mathbf{x}_p$:

$$\begin{bmatrix} x_p \\ y_p \end{bmatrix} = \frac{1}{\det \boldsymbol{\Xi}} \boldsymbol{\Xi} \cdot \boldsymbol{\Sigma}, \tag{60}$$

where

$$\boldsymbol{\Xi} = \begin{bmatrix} (v+v_+)_y + \dfrac{2}{\Delta t} & -(u+u_+)_y \\ -(v+v_+)_x & (u+u_+)_x + \dfrac{2}{\Delta t} \end{bmatrix},$$

$$\boldsymbol{\Sigma} = \begin{bmatrix} \dfrac{\Delta x}{\Delta t} - (u+u_+) \\ \dfrac{\Delta y}{\Delta t} - (v+v_+) \end{bmatrix}.$$

All the quantities in this relation are evaluated at the center of the cell interface. Once the coordinates of $\mathbf{x}_p$ are computed, the solution vector is evaluated at this point.

This procedure is repeated for the manifold $\mathcal{S}_-$ by setting $\mathbf{n} = -\mathbf{n}_s$. The specific curve on $\mathcal{S}_-$ that is used is the one that corresponds to a convective velocity $\mathbf{u}_-$ which satisfies (35). The point at the plane $t = n\Delta t$ that is connected with $(x_w, y_w, (n+1/2)\Delta t)$ by the characteristic equation (24e) is determined by solving numerically the equation (25e), with a procedure similar to the one employed for (25d) that was described earlier. Then, the solution vector is evaluated at this point.

Subsequently, the ODEs (24d) and (24e) are solved for the computation of the pressure and the normal velocity component at the cell interface at time $(n+1/2)\Delta t$. These two equations must be supplemented with appropriate jump conditions when discontinuities are present. Probably the most robust way to implement this, is to treat the discontinuity as if it was normal to the cell interface. This is equivalent to solving an 1-D Riemann problem in the direction parallel to $\mathbf{n}$. Other possible shock directions are also allowed by the algorithm. The 1-D Riemann

problem of the Euler equations for reacting flows is not self-similar like the classical 1-D, gas-dynamic, Riemann problem. Shock waves and expansion fans are not straight lines on the x-t plane anymore, because they are accelerating. Yet, the solution of the Riemann problem for reacting flows converges to the solution of the classical 1-D Riemann problem as $x, t \to 0$, [13]. Therefore, one can safely use the solution of the classical 1-D Riemann problem for computational purposes, see also [11].

As mentioned earlier, allowing discontinuities only at the cell interfaces is a feature not only of this algorithm but of all shock-capturing schemes. This constraint can be important, especially in cases of oblique shocks fronts because it might result to more numerical diffusion than desired. This constraint, however, is independent of the effort to design unsplit schemes, where the goal is to reconstruct the solution by being able to consider information from all possible directions.

The tangential velocity component, $\mathbf{u} \cdot \mathbf{n}^{\perp}$, is evaluated by selecting a curve on $\mathcal{S}_{\perp}$. In the present work, the selected curve corresponds to the velocity $\mathbf{u}_{\perp}$ given by equation (42c). As usual, the curve is approximated by a straight-line segment, and its intersection with the plane $t = n\Delta t$ is computed. At that point, $\mathbf{u} \cdot \mathbf{n}^{\perp}$ has the same value as at $(x_w, y_w, (n+1/2)\Delta t)$. The expression for the coordinates of that point is analogous to (60). The reactant mass fraction is evaluated by selecting a curve on $\mathcal{S}_{\mathrm{r}}$. The selected curve corresponds to a velocity $\mathbf{u}_{\mathrm{r}}$ given by equation (42b).

Finally, the density is evaluated by tracing the curve on $\mathcal{S}_0$ that corresponds to a velocity $\mathbf{u}_0$ given by equation (42a), and subsequently locating the point at which this curve crosses the $t = n\Delta t$ plane. Let p_0,ρ_0 denote the values of pressure and density at this point. The density at the interface, say $(i+1/2, j)$, is evaluated by discretizing equation (24a) in the following way.
If $p^{n+1/2}_{i+1/2,j} > p_0$, then

$$\left(p^{n+1/2}_{i+1/2,j} - p_0\right) - \left((\gamma+1)\,p_0 + (\gamma-1)\,p^{n+1/2}_{i+1/2,j}\right) \frac{\left(\rho^{n+1/2}_{i+1/2,j} - \rho_0\right)}{2\rho_0} = 0. \tag{61a}$$

If $p^{n+1/2}_{i+1/2,j} \le p_0$, then

$$\rho^{n+1/2}_{i+1/2,j} = \rho_0 \left(p^{n+1/2}_{i+1/2,j} / p_0\right)^{1/\gamma}. \tag{61b}$$

Equation (61a) is the jump condition of (24a). It is used when the curve on $\mathcal{S}_0$ is being crossed by a shock. Equation (61b) is just the discretized version of (24a).

The computational costs of this algorithm and the traditional MUSCL scheme [3], equipped with operator splitting, are comparable. This is because the only additional operations needed by the proposed scheme are those for the calculation of the convective velocities $\mathbf{u}_0$, $\mathbf{u}_{\mathrm{r}}$, $\mathbf{u}_{\perp}$, $\mathbf{u}_{+}$, $\mathbf{u}_{-}$. These velocities are computed directly from equations (28), (35), and (42a)–(42c), respectively, without any iterative procedure. Their computation is, therefore, performed at minimal cost.

3. NUMERICAL TESTS OF TWO-DIMENSIONAL DETONATIONS

Detonations are generally unstable phenomena with many spatial and temporal scales. The most noticeable feature of a detonation is the cellular structure, e.g., [14]. These structures are sustained because of the continuous energy release from the chemical reaction. The cells are diamond shaped and are formed by the trajectories of the triple points of the main front. The cell size can be almost uniform, resulting in a system of regularly distributed cells, or it might vary from cell to cell. The existence, or not, of such regularity depends on the combustible mixture and the width of the channel. In general, narrow channels result in cells of uniform size. Unconfined detonations typically produce irregular cellular patterns. It has been observed [14] that the cell spacing is of the order of 100 reaction-lengths of the steady (ZND) solution. The

linearized, two-dimensional stability problem has been considered by [15], who used a Fourier-series approach to investigate the growth-rate of transverse instabilities. For more recent works on the two-dimensional stability problems, see among others, Yao and Stewart [16] and Clavin *et al.* [17].

In general, linearized-stability theories applied to these problems are accurate in the prediction of the stability limits. As it turns out, two-dimensional detonations, governed by one-step Arrhenius kinetics, are intrinsically unstable. Stability is maintained only if the overdrive is high (more than ten), or the activation energy is small. The approximate theories mentioned above, however, have not been successful in the prediction of cell size because the mechanisms that determine the evolution of detonation fronts are highly nonlinear.

Numerical simulation of 2-D detonations was initiated in the early 1970s [18]. More recently, Oran *et al.* [19] simulated detonating flows in rectangular domains with periodic boundary conditions at the top and bottom boundaries using the flux-corrected-transport (FCT) algorithm. Bourlioux and Majda [20] performed simulations of the same problem for a wide range of parameters using the piecewise parabolic method (PPM), see [5]. Cai [21] presented results with a hybrid algorithm that uses an essentially nonoscillatory (ENO) scheme at regimes of steep gradients and spectral representation elsewhere. In the present work, detonations in channels are solved numerically to examine the effectiveness of the proposed algorithm and to make comparisons with previously published results.

3.1. Preliminary Test

This test simulates the flow of a reactive gas over a wedge. The wedge is placed instantly in the uniform flow of the gas and a shock is then formed at the wedge. Since the gas is reactive, the shock is progressively curved due to the dilatation of the reacting material behind the shock. A detonation might be established downstream if the shock temperature is sufficiently high. The wedge is assumed to be long enough so that its geometry downstream cannot influence the flow the computational domain.

The wedge angle θ is an important parameter of this problem. It is expected that for small wedge angles the shock turns smoothly and the flow far downstream consists of a standing oblique ZND wave, i.e., a ZND wave with a nonzero transversal velocity component. Pratt *et al.* [22] studied the parametric values of the wedge angle θ and upstream Mach number M that result in such standing waves. For this test, $\theta = 20^o$. The properties of the gas are

$$\gamma = 1.2, \qquad q_0 = 50.0, \qquad K = 3.125, \qquad E_a = 10.0,$$

while the upstream condition of the gas is

$$p = 1.0, \qquad T = 1.0, \qquad M = 15.0.$$

The theoretical prediction is that downstream the flow reduces to an oblique ZND wave of overdrive factor $f = 1.2$, and at a shock angle of approximately 43.5°. The computational domain is a rectangle with dimensions 120×32 unit lengths (a unit length is the half-reaction length of the ZND wave). The bottom boundary is the wall of the wedge. Inflow conditions have been specified at the left boundary and outflow conditions at the top and right boundaries. Two different mesh sizes have been used, 240×64 and 480×128 cells, respectively.

Contour plots of the flow variables at $t = 25.0$ are shown in Figure 4. At that time the flow has already reached steady state. Each plot contains 15 contours at values equally distributed between the minimum and maximum values of the variables. As expected, the results obtained with the two different resolutions are very close. The smearing of the shock is the only noticeable difference. Simulations of such flows have been performed, among others, by Li *et al.* [23]. Their

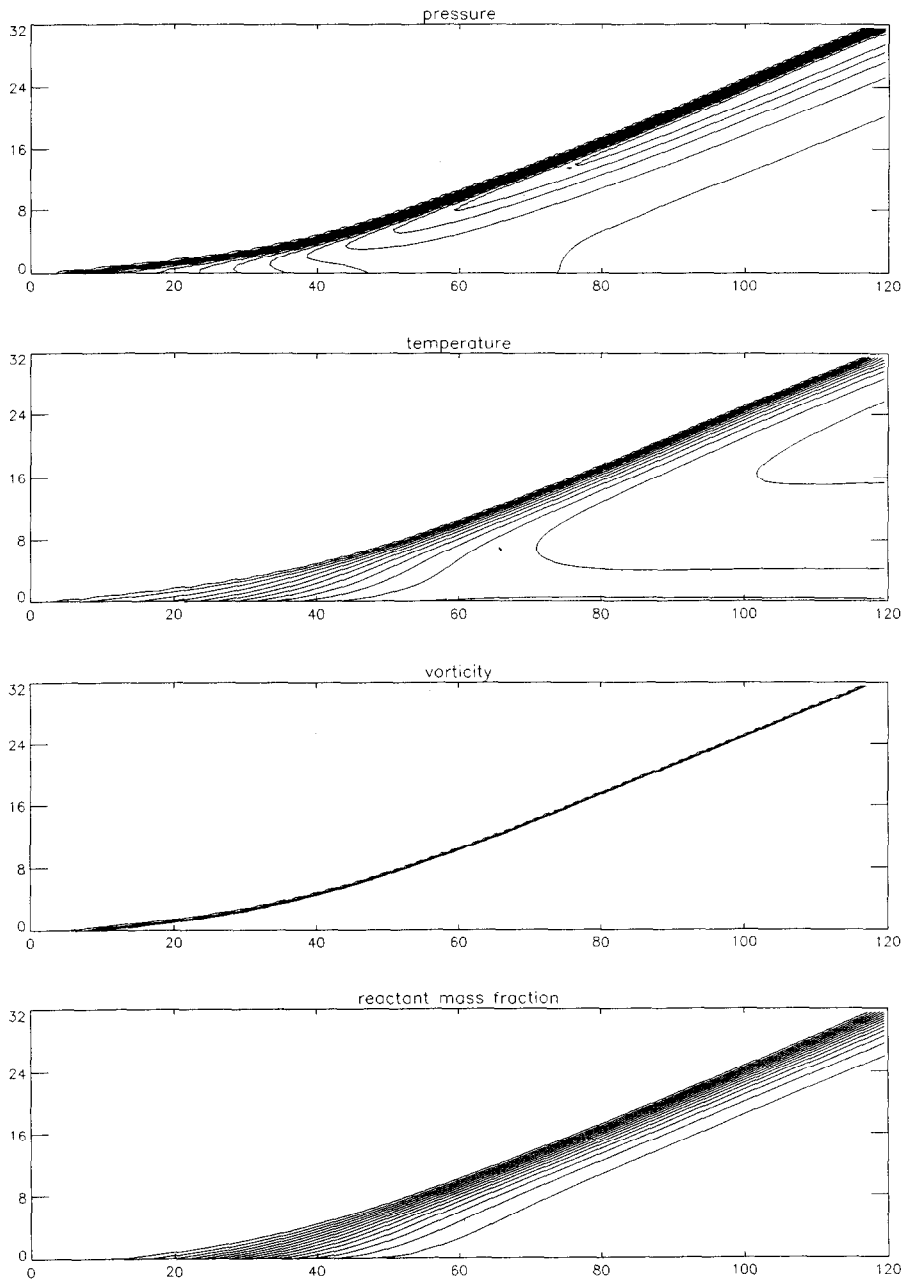

(a) Mesh size, 240 x 64 cells.

Figure 4. Oblique detonation, contour plots of the flow variables at $t = 25.0$.

results were similar to the ones reported here. A detailed study of wedge-induced detonations with the proposed unsplit algorithm is presented in [24].

3.2. Numerical Tests of Detonations in Channel Flows

In this set of numerical tests the computational domain is a rectangle. Periodic conditions are imposed on the top and bottom boundaries and inflow conditions are imposed on the left boundary. Finally, outflow conditions are prescribed on the right boundary. The flow at this boundary is subsonic. The problem of evaluating the fluxes across a boundary becomes underdetermined when one or more curves of the invariant manifolds lie outside the computational

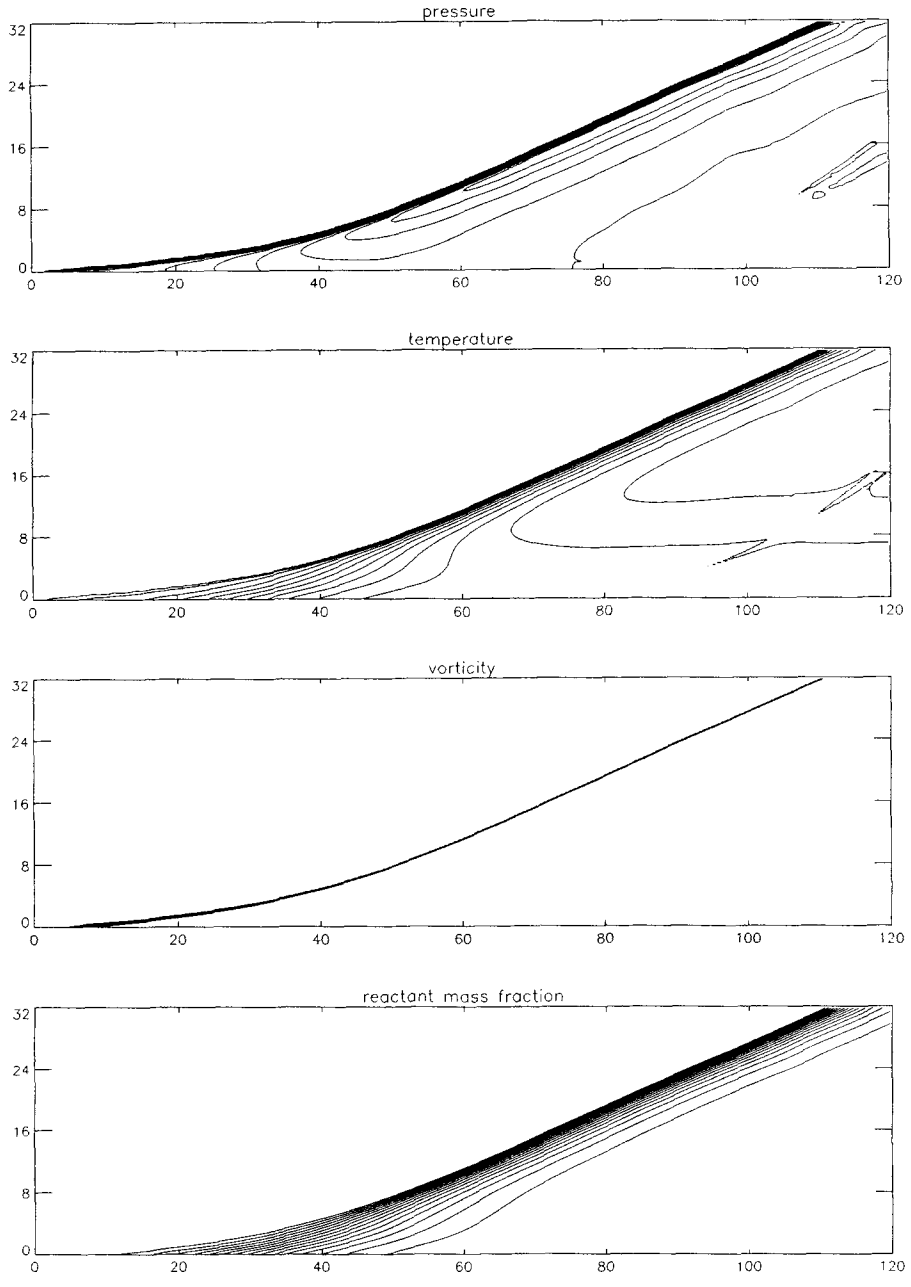

(b) Mesh size, 480 x 128 cells.

Figure 4. (cont.)

domain. Therefore, an *a priori* condition needs to be imposed, but in such way that no artificial wave-reflections occur at the boundary. In the present work, this is achieved by copying the values from the boundary cells to their corresponding dummy cells. By doing so, two conditions are satisfied. First, all the invariant curves lie inside the computational domain except for the curve defined by (25e) which lies outside. Second, each term of the characteristic equation (24e) that holds on (25e) becomes identically 0, thus overcoming the underdeterminacy problem.

The initial condition is a transversally-perturbed, planar ZND wave, propagating in a quiescent medium. For a given choice of parameters the one-dimensional ZND profile has been computed numerically and it is assigned to each longitudinal station throughout the width of the domain.

The perturbation is a sinusoidal variation of the amplitude of the post-shock values of the flow variables in the transversal direction. It is employed to trigger the instabilities faster than the truncation error would. The ZND wave is assumed to propagate to the left and is stationary with respect to the laboratory frame. Hence, if the flow was indeed steady the position of the shock front would be constant in this frame.

It is a common practice to employ explicit artificial dissipation mechanisms for compressible flow simulations. This is often necessary because the implicit viscosity of the scheme, which arises from the discretization of the equations and monotonicity constraints, is not adequate for the stabilization of strong shocks. For a detailed discussion on this topic, see [5]. The only explicit dissipation mechanism that has been employed in the proposed unsplit scheme is slope limiting, even though the leading shock fronts in detonations are typically quite strong (the shock Mach number is typically above ten). Additional explicit dissipation has been employed in most of the previously published results of two-dimensional detonations. The extra dissipation was used in the vicinity of either the leading shock or the transverse shock waves.

Furthermore, if a shock is sufficiently slow with respect to the grid, Godunov-type schemes generate spurious post-shock oscillations. These oscillations occur because one eigenvalue of the equations changes sign across the shock, see [5]. The change of sign makes the diffusive term of the difference equations that approximate the original system, locally very small. Therefore, additional artificial dissipation is needed to suppress the oscillations. In two-dimensional problems, this error is smaller because flow obliquity introduces the required dissipation and because the error can diffuse away from the front in other directions. In the simulations presented here, the front is initially planar and is moving slowly with respect to the grid in the early stages of the process. The amplitude of the resulting error, however, is small because of the transverse perturbations in the initial condition. These perturbations introduce fluxes to the y-direction,

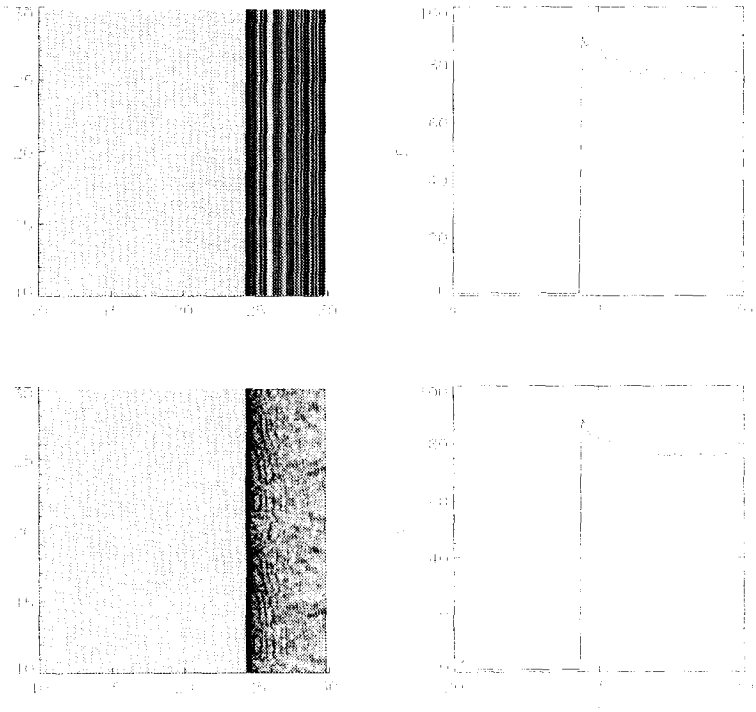

Figure 5. Pressure field for a planar detonation, at $t = 3.0$ Schlieren-type images and plots along the centerline with initial transverse perturbation (bottom row), and without (top row). Two periods in the y-direction are plotted.

making the flow two-dimensional even at small times. If these perturbations had not been introduced, then persistent post-shock oscillations would have been generated.

To illustrate this effect, Schlieren-type snapshots of the pressure field and plots of the pressure along the bottom boundary for both initial conditions (with and without perturbations) are

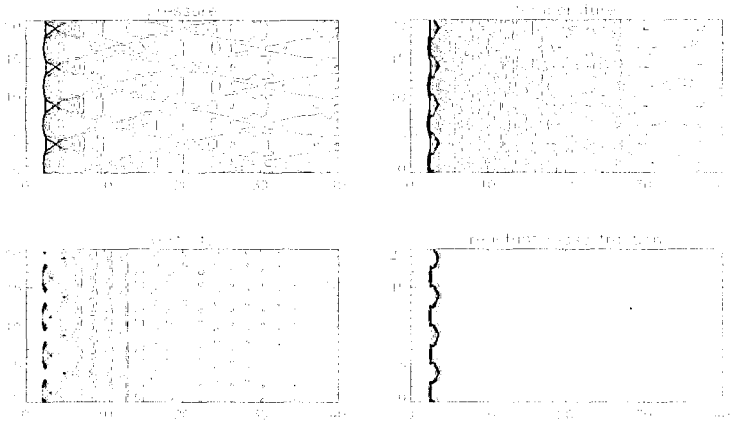

(a) Resolution: ten points per unit length.

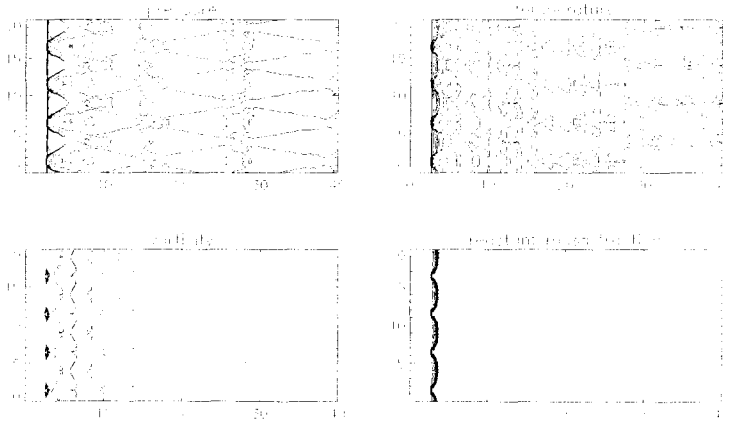

(b) Resolution: 20 points per unit length.

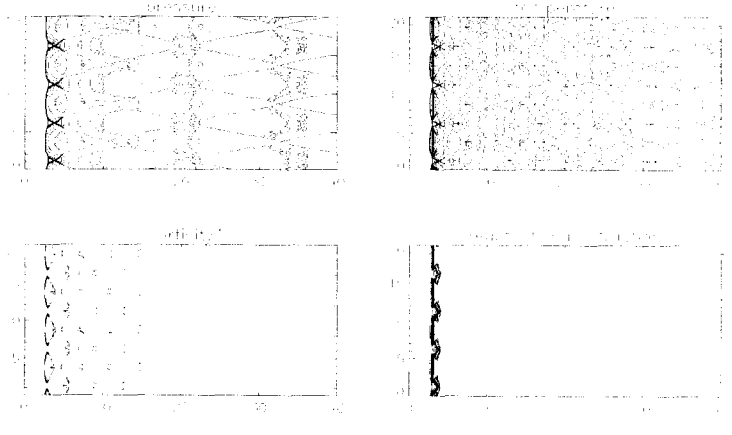

(c) Resolution: 30 points per unit length.

Figure 6. Case A: contour plots of the flow variables at $t = 60.0$. Two periods in the y-direction are plotted.

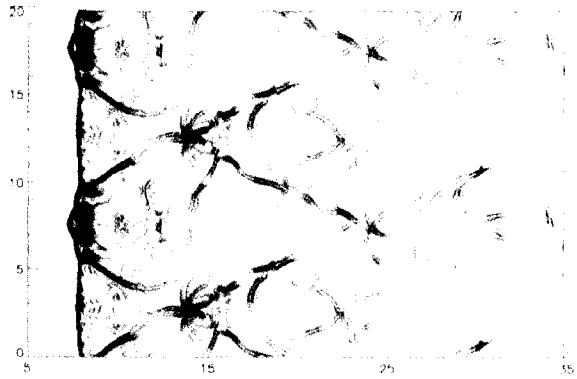

(a) Pressure.

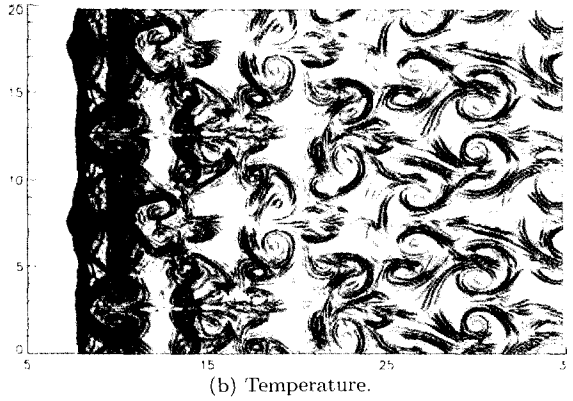

(b) Temperature.

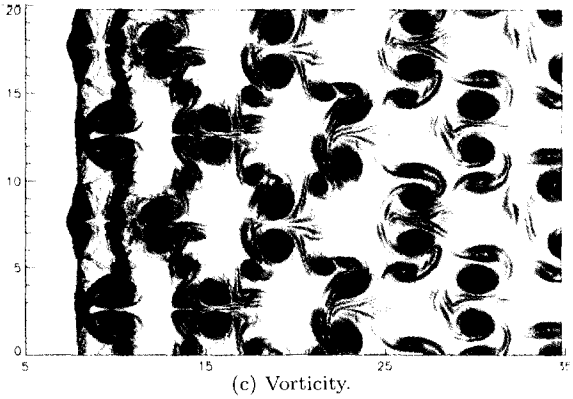

(c) Vorticity.

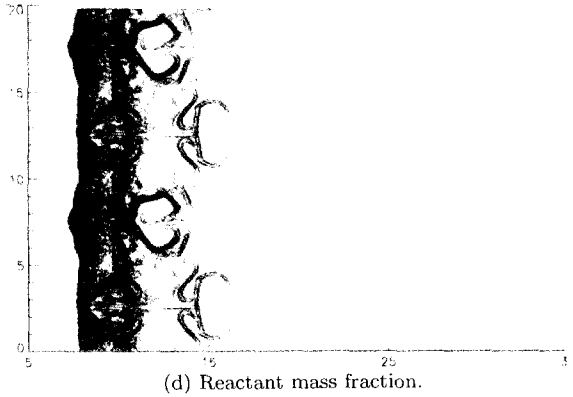

(d) Reactant mass fraction.

Figure 7. Case B. Schlieren-type images of flow variables at $t = 60.0$. Two periods in the y-direction are plotted.

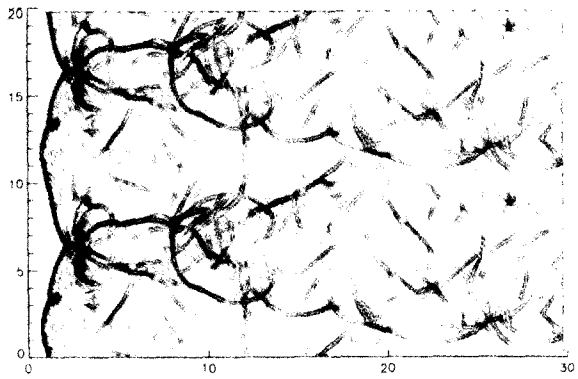

(a) Pressure.

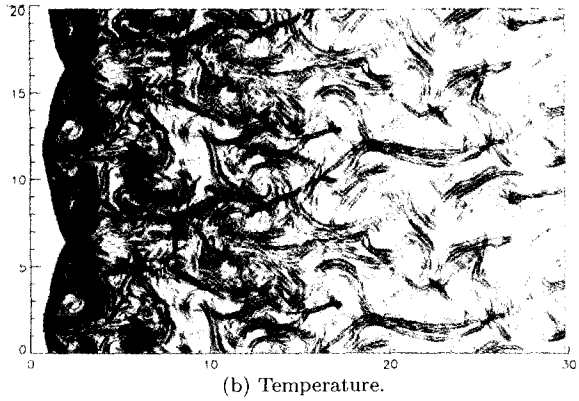

(b) Temperature.

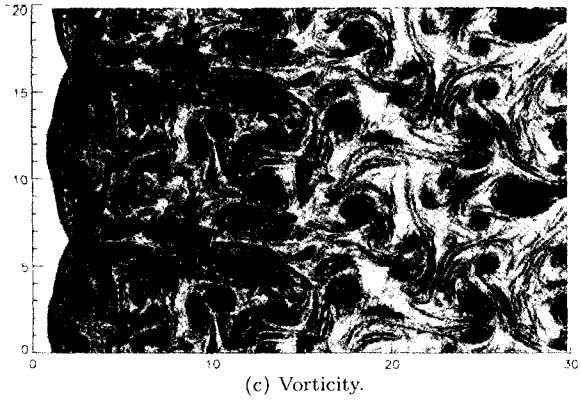

(c) Vorticity.

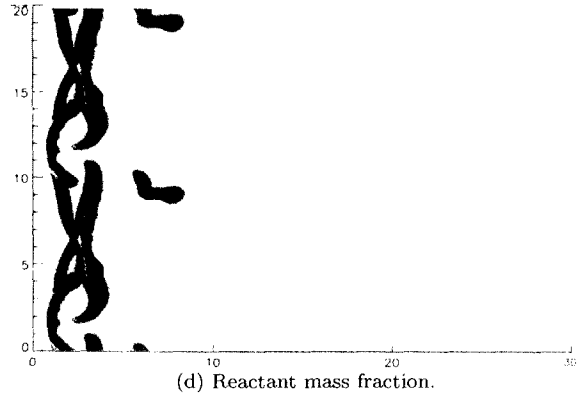

(d) Reactant mass fraction.

Figure 8. Case C. Schlieren-type images of flow variables at $t = 40.0$. Two periods in the y-direction are plotted.

presented in Figure 5, for comparison. The detonation parameters are: $\gamma = 1.2$, $E_a = 50.0$, $q_0 = 50.0$, and $f = 1.6$. These snapshots are taken at $t = 3.0$. The shock is initially located at $x = 25.0$. The expression "Schlieren-type snapshot" implies snapshots of the norm of the gradient vector of a variable. Once the instabilities are fully developed and the cellular structure is formed, the front moves fast with respect to the grid and the local curvature of the front can be substantial. Therefore, post-shock oscillations are strongly diminished in the later stages of the process.

Results for three different cases are presented. In all cases, the variables and parameters of the system have been made dimensionless by reference to the uniform state ahead of the detonation front. The half-reaction length of the ZND profile, $L_{1/2}$, is characteristic length-scale. $L_{1/2}$ divided by the sound speed ahead of the shock provides the characteristic time scale. The spatial resolution is, unless otherwise specified, 20 points per half-reaction length, and the CFL number has been set at CFL = 0.7. The sinusoidal transversal perturbation of a variable has an amplitude equal to 0.2% of its post-shock value. The wavelength of the perturbation is one unit-length.

CASE A. This is a case of low activation energy and low heat release,

$$\gamma = 1.2, \qquad E_a = 20.0, \qquad q_0 = 2.0, \qquad f = 1.2.$$

The stiffness coefficient of the system is $K = 1134363.64$. The computational domain of the simulation is 30 unit-lengths long and ten unit-lengths wide. The ZND wave is initially located at $x = 35.0$.

The corresponding one-dimensional case is linearly stable, i.e., there are no linearly unstable longitudinal modes. The transverse perturbations, however, grow and transverse waves are eventually generated. These waves lead to the formation of the familiar cellular structures. As mentioned earlier, the explosions generated by the collisions of the transverse waves release large amounts of heat that allow the conservation of these patterns. In this particular case, the collisions occur periodically in time. The cellular structures are quite regular and have the same size. The geometry of the main front also changes periodically. The dimensionless shock pressure, according to the ZND solution, is $p_s = 3.688$. In the numerical simulation, the shock pressure goes as high as $p_s = 6.1267$.

Results for this case at time $t = 160.0$ are presented in Figure 6b. They agree well with the results presented in [20]. The structure of the main front, in particular, and the cellular patterns are the same in both simulations. Different resolutions, namely ten and 30 points per unit-length, have also been used. These results are shown in Figures 6a and 6c, respectively. The flow-fields generated by the three simulations are very similar. The patterns of the flow field are stable in time and space with regard to resolution. The main difference is that the vorticity structures become sharper as the resolution is increased.

CASE B. In this case, both the activation energy and the overdrive factor are low,

$$\gamma = 1.2, \qquad E_a = 10.0, \qquad q_0 = 50.0, \qquad f = 1.2.$$

The stiffness coefficient for this case is $K = 3.124$. The computational domain is 60 unit-lengths long and ten unit-lengths wide, i.e., it consists of 1200×200 points. The initial ZND wave is placed at $x = 55.0$. The corresponding one-dimensional flow is stable. The CFL number has been lowered to 0.3. Such a low value is necessary to avoid excessive numerical diffusion that may smear important flow patterns.

Results for this case are presented in Figure 7. The simulations show that the structure of the main front varies periodically with time. The transverse waves are weaker and shorter than those of the previous cases. The vortex sheets from two colliding triple points detach from the front simultaneously, thus forming pairs. These pairs are regularly distributed in the wake of the front. The shock pressure of the ZND solution is $p_s = 50.49$, but the maximum shock pressure of the simulation is $p_s = 144.62$. The numerical simulations show that the structure of the main

front varies periodically with time. The results obtained with the proposed algorithm are in very good agreement with the results presented in [20] for the same case.

CASE C. This is a case of low overdrive factor and high heat release. The corresponding one-dimensional problem has five unstable longitudinal modes,

$$\gamma = 1.2, \qquad E_a = 50.0, \qquad q_0 = 50.0, \qquad f = 1.2.$$

The stiffness coefficient for this detonation is $K = 871.42$. The computational domain of the simulation is 60 unit-lengths long and ten unit-lengths wide. The initial ZND wave is located at $x = 5.0$. Schlieren-type snapshots of the flow variables for this problem are given in Figure 8.

The two-dimensional analysis in [15] reveals that this detonation is unstable at arbitrarily short wavelengths. In the early stages, the evolution of the flow-field resembles the equivalent one-dimensional process. More specifically, the shock pressure and temperature drop below the ZND values and, as a consequence, the reaction zone stays temporarily behind the hydrodynamic shock. Later on, material burns fast due to thermal runaway, resulting to high over-pressures. This similarity to the one-dimensional case suggests that in early times the evolution process is dominated by longitudinal instabilities.

Once the transverse instabilities grow and start dominating the flow, the structures of the flow field become very complicated. At the front, strong triple-point collisions occur, generating new systems of shock waves. In the wake of the front, there are many vortical structures. Pockets of unreacted material are constantly created and subsequently burn. They are long chunks of unburnt material, almost parallel to the main front. Sometimes they can span the width of the channel.

The transverse waves of the triple points are strong and can be more than ten lengths long. Transverse-wave collisions are encountered often. The shock wave systems that result from these collisions interact with the vortical structures that have been convected downstream from the main front. There is no evidence of regularity even far behind the leading front. According to the ZND theory, the shock pressure is $p_s = 50.49$. In the present simulation, the maximum value observed is $p_s = 220.0$. Results for this case have also been reported in [20], where similar phenomena were observed. The main features of the flow (long unreacted pockets, strong vortical interaction in the wake, etc.) are the same in both simulations.

4. CONCLUDING REMARKS

A new shock-capturing, MUSCL-type algorithm has been proposed for the numerical study of multidimensional systems of hyperbolic conservation laws with source terms. The algorithm is fully unsplit in the sense that it avoids both dimensional and time splitting. It is based on the decomposition of the governing system to the set of equations that is satisfied along the characteristic paths of the corresponding 1-D homogeneous problem. Each of these equations now holds along a specific space-time manifold, referred to as a Riemann invariant manifold. Numerical integration of these equations is performed in the upwinding step of the algorithm.

The performance of the proposed algorithm was tested via simulations of stable and unstable two-dimensional detonations. The stable cases were a wedge-induced detonation, and a planar detonation of low activation energy and heat release. In both cases, numerical convergence was observed as the grid was refined. The unstable cases were two examples of planar detonations with large heat release. Such flows are characterized by cellular structures that are formed by the motion of the triple points of the leading shock. The slip lines emanating from these points roll up, detach from the front, and interact with the wave structures of the wake. The proposed algorithm appeared to be stable and capable of capturing many important details of the flow-fields. No special treatment other than slope-limiting was employed to suppress spurious oscillations and to avoid entropy-violating shocks. In particular, flux-splitting and entropy-fixes were completely avoided with the proposed method.

REFERENCES

1. J. Glimm, Solutions in the large for nonlinear hyperbolic systems of equations, *Comm. Pure Appl. Math.* **18**, 35, (1965).
2. P. Lax, Hyperbolic systems of conservation laws and the mathematical theory of shock waves, *SIAM*, (1973).
3. B. van Leer, Towards the ultimate conservative difference scheme, V. A second order sequel to Godunov's method, *J. Comp. Phys.* **32**, 101, (1979).
4. A. Harten, B. Engquist, S. Osher and S. Chakravarthy, Uniformly high order accurate ENO schemes, III, *J. Comp. Phys.* **71**, 231, (1987).
5. P. Colella and P.R. Woodward, The PPM method for gas dynamic simulations, *J. Comp. Phys.* **54**, 174, (1984).
6. H. Deconick, C. Hirsch and J. Peuteman, Characteristic decomposition methods for the multidimensional Euler equations, 10^{th} International Conference on Numerical Methods Bejing in Fluid Dynamics, AIAA paper No. 89-1958, (1986).
7. P. Colella, Multidimensional upwind methods for hyperbolic conservation laws, *J. Comp. Phys.* **87**, 171, (1988).
8. L.J. Leveque, High resolution finite volume methods on arbitrary grids via wave propagation, *J. Comp. Phys.* **78**, 33, (1988).
9. W.L. Dai and P.R. Woodward, A 2^{nd} order unsplit Godunov scheme for 2-dimensional and 3-dimensional Euler equations, *J. Comp. Phys.* **134**, 261, (1997).
10. T. Lappas, A. Leonard and P.E. Dimotakis, Riemann invariant manifolds for the multidimensional Euler equations, *SIAM J. Sci. Comp.* **20**, 1481, (1999).
11. M.V. Papalexandris, A. Leonard and P.E. Dimotakis, Unsplit schemes for hyperbolic conservation laws with source terms in one space dimension, *J. Comp. Phys.* **134**, 31, (1997).
12. B. van Leer, On the relation between the upwind-differencing schemes of Godunov, Engquist-Osher and Roe, *SIAM J. Sci. Stat. Comp.* **5**, 1, (1984).
13. M. Ben-Artzi, The generalized Riemann problem for reactive flows, *J. Comp. Phys.* **81**, 744, (1989).
14. W. Fickett and W.C. Davis, *Detonation*, U.C. Berkeley Press, (1979).
15. J.J. Erpenbeck, Stability of idealized one-reaction detonations, *Phys. Fluids* **7**, 684, (1964).
16. J. Yao and J.S. Stewart, On the dynamics of multi-dimensional detonations, *J. Fl. Mech.* **309**, 225, (1996).
17. P. Clavin, L. He and F.A. Williams, Multi-dimensional stability analysis of overdriven gaseous detonations, *Phys. Fl.* **9**, 3764–3785, (1997).
18. S. Taki and T. Fujiwara, Numerical analysis of two-dimensional non-steady detonations, *AIAA Journal* **16**, 73, (1973).
19. E.S. Oran, K. Kailasanath and R.H. Guirguis, Numerical simulations of the development and structure of detonations, *Prog. Aeronaut. Astronaut.* **114**, 155, (1988).
20. A. Bourlioux and A.J. Majda, Theoretical and numerical structure for unstable two-dimensional detonations, *Combust. Flame* **90**, 211, (1992).
21. W. Cai, High-order hybrid numerical simulations of 2-dimensional detonation waves, *AIAA Journal* **33**, 1248, (1995).
22. D.T. Pratt, J.W. Humphrey and D.E. Glenn, Morphology of standing oblique detonation waves, *J. Prop. Power* **7**, 837, (1991).
23. C. Li, K. Kailasanath and E.S. Oran, Detonation structures behind oblique shocks, *Phys. Fluids* **6**, 1600, (1994).
24. M.V. Papalexandris, Numerical study of wedge-induced detonations, *Combustion and Flame* **120**, 526, (2000).
25. H.O. Barthel, Reaction zone—Shock front coupling in detonations, *Phys. Fluids* **15**, 43, (1972).